International Journal of Non-Linear Mechanics 121 (2020) 103455

Contents lists available at ScienceDirect

International Journal of Non-Linear Mechanics

journal homepage: www.elsevier.com/locate/nlm

Review

Exploiting nonlinearity to enhance the sensitivity of mode-localized mass sensor based on electrostatically coupled MEMS resonators

Ming Lyu [a], Jian Zhao [a,*], Najib Kacem [b], Pengbo Liu [a], Bin Tang [c], Zhuang Xiong [c], Hongxi Wang [d], Yu Huang [a,e]

[a] State Key Laboratory of Structural Analysis for Industrial Equipment, Dalian University of Technology, Dalian, China
[b] Univ. Bourgogne Franche-Comté, FEMTO-ST Institute, UMR 6174, CNRS/UFC/ENSMM/UTBM, Department of Applied Mechanics, Besançon, France
[c] Institute of Electronic Engineering, China Academy of Engineering Physics, Mianyang, China
[d] School of Mechatronics, Xi'an Technological University, Xi'an, China
[e] College of Ocean and Civil Engineering, Dalian Ocean University, Dalian, China

ARTICLE INFO

Keywords:
Mass sensor
Mode localization
Electrostatic coupling
Nonlinear dynamics

ABSTRACT

An ultrasensitive mass sensor is proposed by combining the benefits of mode localization and nonlinear dynamics in two clamped–clamped microbeams of different lengths. The coupling electrostatic stiffness between the two resonators can be tuned for modulating sensitivity, and the actuation voltage applied to the shorter beam can be adjusted in order to overcome mechanical defects such as geometric asymmetry. The analytical dynamic model considering the quadratic and cubic nonlinearities is established and solved by the asymptotic numerical method (ANM) combined with harmonic balance method (HBM), as well as validated by the long-time integration (LTI) method. A parametric study is performed in order to investigate the effects of the coupling voltage, gap ratio, position of added mass and length ratio on the device sensitivity. Beyond the critical Duffing amplitude and while taking advantage of mode localization, it is shown that the device sensitivity in terms of amplitude ratio is significantly enhanced with up to three orders of magnitude higher than the relative shift in resonance frequencies. The proposed model can be used as a design tool to tune the nonlinearity level enabling the performance improvement of multimodal MEMS mass sensors.

Contents

1. Introduction 2
2. Model 2
   2.1. Dynamic modeling of the electrostatically coupled microbeams 2
   2.2. Static analysis 3
   2.3. Mode veering analysis 4
   2.4. HBM+ANM for periodic solutions 4
3. Numerical results 5
   3.1. Linear behaviors 5
   3.2. Nonlinear behavior 6
   3.3. Adjustability of the sensitivity by electrostatic coupling stiffness 7
4. Influences of the geometric parameters 7
   4.1. Effects of the position of added mass on sensitivity 7
   4.2. Effects of the length ratio on sensitivity 7
   4.3. Effects of the gap ratio on sensitivity 7
5. Conclusion 9
   Declaration of competing interest 9
   CRediT authorship contribution statement 9
   Acknowledgments 9
   Appendix 9
   A.1. Reduced order model 9

* Corresponding author.
E-mail address: Jzhao@dlut.edu.cn (J. Zhao).

https://doi.org/10.1016/j.ijnonlinmec.2020.103455
Received 20 November 2019; Received in revised form 12 February 2020; Accepted 13 February 2020
Available online 25 February 2020
0020-7462/© 2020 Elsevier Ltd. All rights reserved.

A.2. The integration parameters of Eq. (14) 10
References 10

1. Introduction

Mass sensing is one of the most valuable engineering applications for electromechanical resonators, which can be used for measuring and identifying proteins [1,2], DNA [3,4], gas [5], cancer [6] and biomolecules [7]. Sensitivity for mass detection has been regarded as the main decisive characteristic for evaluating the sensor's performance. Hence, a series of sensitivity improving methods have been proposed by means of structure optimization [7,8], dimension miniaturization [1–6], and utilization of nonlinear vibrations [9–12]. For example, Zhao et al. [8] presented a novel design of the resonant mass sensor to improve the sensitivity through configuration integrated optimization. Kacem et al. [9] proposed a carbon nanotube as a resonant cantilever and establishes a nonlinear model to simultaneously detect the mass and position of attached particles. Zhang et al. [10] proposed a nonlinear mass sensing concept based on parametric resonance amplification, which is experimentally validated by a non-interdigitated comb-finger driven micro-oscillator. All these methods are applicable for single-resonator based sensors, which are not immune to ambient interferences.

Recently, the mode localization of at least two weakly coupled resonators has been introduced in mass sensors to enhance the sensitivity and anti-jamming performance [13]. By using such a phenomenon, a small perturbation will cause symmetry-breaking that leads to a drastic shift in eigenstates or amplitude [14,15]. Actually, such symmetric coupled structures involving elastic springs [16,17] or electrostatic couplings [18,19] have been utilized in many sensing applications like mass sensors [20], accelerometers [21] and force sensors [22]. Spletzer et al. [14] introduced two elastic coupled cantilevers in the design of ultrasensitive mass sensors, and it is verified that the sensitivity can be improved over two orders of magnitude compared to the relative change of resonance frequency. The effects of different coupling strengths on the sensitivity of elastic spring coupled resonant mass sensor has been investigated in [23]. Furthermore, the localization of resonator arrays has been studied in several references [24–26], these pieces of literature analyze the influencing factors of the localization in array structures, and provide a research basis for potential sensing applications. Wang et al. [27] proposed a 5-beam array of elastically coupled resonators which shows theoretically three to four times of amplitude shift enhancement compared to a single resonator.

Compared to mechanical coupled structures, the electrostatic coupling structures of variable stiffness have great potentials in designing adjustable sensors to enhance their environment adaptability. Thiruvenkatanathan et al. [19] utilized the electrostatic coupling to obtain a lower coupling stiffness and hence improve sensitivity for mode-localized resonators. Zhao et al. [28] used the electrostatic coupling to design a novel 3DoF weakly coupled structure to be used as a mode localization sensor, and its sensitivity has been dramatically improved compared with 2DoF mode localization resonant sensors. Pandit et al. [29] investigated the improvement of resolution gains of electrostatic coupling nonlinear resonators compared with the linear counterpart. In addition to significantly improving sensitivity, mode localization resonators are also robust to environmental disturbances. In [30], the eigenstates shift remains relatively constant at different environment pressures and temperatures. The robustness of mode localization readouts has been verified sufficiently by Zhang et al. [13], and the results showed that the amplitude ratio can reject the ambient pressure drift. These sensors are based on exactly identical resonators, and the devices are initially balanced. However, as the size of the structure decreases, manufacturing error induced asymmetrical items will significantly unbalance the system resulting in malfunction.

Rabenimanana et al. [15] proposed a mass sensor with two weakly coupled cantilevers with different lengths, which provided an effective way to overcome the influence of the non-negligible mechanical defects, but limited to linear vibrations. In this paper, an ultrasensitive mass sensor is proposed by introducing mode localization in two weakly coupled microbeams of different lengths while combining the benefits of nonlinear dynamics and electrostatic coupling. The latter can be tuned to achieve variable stiffness and enables sensitivity improvement. The short beam is actuated by a combined AC–DC voltage. The dynamic analytical model considering the quadratic and cubic nonlinearities is established by using the Galerkin method. The dynamic response is obtained by using the asymptotic numerical method (ANM) with harmonic balance method (HBM), and the validation is performed with respect to solutions obtained using long-time integration (LTI) method. For the electrostatic weakly coupled microbeams, and while using the amplitude ratio as the output metric, the sensitivity can be improved by three orders of magnitude compared to the frequency shift output metric. For adjustability, the mass sensor can be controlled to operate in the linear and nonlinear vibrations by regulating the actuating voltage. It is shown that the sensitivity is significantly enhanced when the device is driven beyond its critical Duffing amplitude compared to the linear regime. Finally, the effects of specific design parameters on the device sensitivity are investigated while ensuring nonlinear vibrations under primary resonance.

The present paper is organized as follows: the motion equations of the structure are proposed in Section 2. In Section 3, the results of the system operating in the linear and nonlinear states are studied. In Section 4, the influence of the different parameters on the sensitivity is investigated. Finally, conclusions are collected in Section 5.

2. Model

The proposed mass sensor is composed of two clamped–clamped microbeams coupled by the bias voltage V_c as sketched in Fig. 1. The two microbeams have different lengths and only the shorter microbeam 2 is actuated by a combined voltage $V_a(\tilde{t}) = V_{dc} + V_{ac}cos(\tilde{\Omega}\tilde{t})$ in the bottom, where V_{dc} and V_{ac} are the DC polarization voltage and the applied AC voltage, $\tilde{\Omega}$ is the excitation frequency. The actuation voltage applied to the shorter microbeam can be adjusted to overcome the mechanical defects of asymmetric microbeams having unequal lengths. The design parameters of the system are given in Table 1.

2.1. Dynamic modeling of the electrostatically coupled microbeams

The governing equations of motion of the two coupled microbeams are established by using the Euler–Bernoulli theory.

$$\begin{aligned}
&EI\frac{\partial^4\tilde{w}_1(\tilde{x},\tilde{t})}{\partial\tilde{x}^4}+\rho A\frac{\partial^2\tilde{w}_1(\tilde{x},\tilde{t})}{\partial\tilde{t}^2}+\delta_{\tilde{x}_0}(\tilde{x}-\tilde{x}_0)\,m_p\frac{\partial^2\tilde{w}_1(\tilde{x},\tilde{t})}{\partial\tilde{t}^2}\\
&+\tilde{c}\frac{\partial\tilde{w}_1(\tilde{x},\tilde{t})}{\partial\tilde{t}}-\left[\tilde{N}_1+\frac{EA}{2l_1}\int_0^{l_1}\left(\frac{\partial\tilde{w}_1(\tilde{x},\tilde{t})}{\partial\tilde{x}}\right)^2d\tilde{x}\right]\frac{\partial^2\tilde{w}_1(\tilde{x},\tilde{t})}{\partial\tilde{x}^2}=\\
&-\frac{1}{2}\frac{\varepsilon_0 bV_c^2}{\left(g_c+\tilde{w}_1(\tilde{x},\tilde{t})-\tilde{w}_2(\tilde{x},\tilde{t})\right)^2}H_1(\tilde{x})
\end{aligned}\tag{1}$$

$$\begin{aligned}
&EI\frac{\partial^4\tilde{w}_2(\tilde{x},\tilde{t})}{\partial\tilde{x}^4}+\rho A\frac{\partial^2\tilde{w}_2(\tilde{x},\tilde{t})}{\partial\tilde{t}^2}+\tilde{c}\frac{\partial\tilde{w}_2(\tilde{x},\tilde{t})}{\partial\tilde{t}}\\
&-\left[\tilde{N}_2+\frac{EA}{2l_2}\int_{\frac{l_1-l_2}{2}}^{\frac{l_1+l_2}{2}}\left(\frac{\partial\tilde{w}_2(\tilde{x},\tilde{t})}{\partial\tilde{x}}\right)^2d\tilde{x}\right]\frac{\partial^2\tilde{w}_2(\tilde{x},\tilde{t})}{\partial\tilde{x}^2}
\end{aligned}$$

Table 1
Design parameters of the proposed mass sensor.

Parameter	Value (μm)	Parameter	Value
Length of microbeam 1 (l_1)	200	Young's modulus (E)	160 GPa
Length of microbeam 2 (l_2)	192	Density (ρ)	2330 kg/m^3
Microbeam width (b)	4	Air gap (g_a)	1 μm
Microbeam height (h)	1	Air gap (g_c)	2 μm

$$= \frac{1}{2}\frac{\varepsilon_0 b V_c^2}{\left(g_c+\widetilde{w}_1\left(\widetilde{x},\widetilde{t}\right)-\widetilde{w}_2\left(\widetilde{x},\widetilde{t}\right)\right)^2}H_1\left(\widetilde{x}\right)-\frac{1}{2}\frac{\varepsilon_0 b\left[V_{dc}+V_{ac}\cos\left(\widetilde{\Omega}\widetilde{t}\right)\right]^2}{\left(g_a+\widetilde{w}_2\left(\widetilde{x},\widetilde{t}\right)\right)^2} \tag{2}$$

where H_1 is the Heaviside function, δ the Dirac function.

$$H_1\left(\widetilde{x}\right)=\left|H\left(\widetilde{x}-\frac{l_1-l_3}{2}\right)-H\left(\widetilde{x}-\frac{l_1+l_3}{2}\right)\right| \tag{3}$$

and the boundary conditions of the microbeams are

$$\begin{cases}\widetilde{w}_1\left(0,\widetilde{t}\right)=\widetilde{w}_1\left(l_1,\widetilde{t}\right)=\dfrac{\partial\widetilde{w}_1}{\partial\widetilde{x}}\left(0,\widetilde{t}\right)=\dfrac{\partial\widetilde{w}_1}{\partial\widetilde{x}}\left(l_1,\widetilde{t}\right)\\ \widetilde{w}_2\left(\dfrac{l_1-l_2}{2},\widetilde{t}\right)=\widetilde{w}_2\left(\dfrac{l_1+l_2}{2},\widetilde{t}\right)=\dfrac{\partial\widetilde{w}_2}{\partial\widetilde{x}}\left(\dfrac{l_1-l_2}{2},\widetilde{t}\right)\\ \quad=\dfrac{\partial\widetilde{w}_2}{\partial\widetilde{x}}\left(\dfrac{l_1+l_2}{2},\widetilde{t}\right)\end{cases} \tag{4}$$

where $\widetilde{x}$ is the position along the microbeam length, $\widetilde{t}$ is time, $\widetilde{c}$ is the linear viscous damping per unit length, E is the Young modulus, ρ is the mass density, $I=bh^3/12$ is the moment of inertia, b, h is the width and the thickness, respectively, g_c and g_a are two gap distances, l_1 and l_2 are two lengths of microbeam 1 and microbeam 2, l_3 is the length of the electrode on microbeam 1, $\widetilde{w}_1$ and $\widetilde{w}_2$ are the transverse deflections of the microbeam 1 and microbeam 2, A is microbeam cross-sectional area, ε_0 is the dielectric constant of the gap medium, m_p is added mass, V_c is the applied voltage on the coupling electrode.

For simplicity, the governing equations of the system will be normalized by the following non-dimensional parameters

$$w_1=\frac{\widetilde{w}_1}{g_a},x=\frac{\widetilde{x}}{l_1},t=\frac{\widetilde{t}}{\tau},w_2=\frac{\widetilde{w}_2}{g_a},\Lambda=\frac{l_2}{l_1},R=\frac{g_c}{g_a} \tag{5}$$

where $\tau=\sqrt{\frac{\rho A l_1^4}{EI}}$.

Substituting Eq. (5) into Eqs. (1)–(4) dropping the hats. To reduce the computational complexity of the equations, the electrostatic force terms have been expanded in Taylor series in Eqs. (1) and (2). In [31], it is found that the accuracy of using the truncated Taylor series is greatly affected by the response amplitude. Since the two microbeams only operate at small amplitudes ($\widetilde{w}_1,\widetilde{w}_2<0.1$) in this paper, third-order Taylor expansion is used for the electrostatic actuation force term to obtain up to three possible amplitudes for a given frequency [32]. As the coupling voltage is very weak, its corresponding electrostatic forces in Eqs (1) and (2) have been expanded into first order Taylor series.

$$\begin{cases}\dfrac{\partial^4 w_1}{\partial x^4}+\dfrac{\partial^2 w_1}{\partial t^2}+\delta_{x_0}(x)\Delta m\dfrac{\partial^2 w_1}{\partial t^2}-\left[N_1+\alpha_1\displaystyle\int_0^1\left(\dfrac{\partial w_1}{\partial x}\right)^2dx\right]\dfrac{\partial^2 w_1}{\partial x^2}\\ =-c\dfrac{\partial w_1}{\partial t}-\alpha_2 V_c^2 H_1(x)\left(\dfrac{1}{R^2}-\dfrac{2}{R^3}\left(w_1-w_2\right)\right)\\ \dfrac{\partial^4 w_2}{\partial x^4}+\dfrac{\partial^2 w_2}{\partial t^2}+c\dfrac{\partial w_2}{\partial t}-\left[N_2+\alpha_3\displaystyle\int_{\frac{1-\Lambda}{2}}^{\frac{1+\Lambda}{2}}\left(\dfrac{\partial w_2}{\partial x}\right)^2dx\right]\dfrac{\partial^2 w_2}{\partial x^2}=\\ -\alpha_2\left[V_{dc}+V_{ac}\cos(\Omega t)\right]^2\left(1-2w_2+3w_2^2-4w_2^3\right)\\ +\alpha_2 V_c^2 H_1(x)\left(\dfrac{1}{R^2}-\dfrac{2}{R^3}\left(w_1-w_2\right)\right)\end{cases} \tag{6}$$

The expressions of the non-dimensional parameters are defined

$$c=\frac{\widetilde{c}l_1^4}{EI\tau},N_1=\frac{\widetilde{N}_1 l_1^2}{EI},N_2=\frac{\widetilde{N}_2 l_1^2}{EI},\alpha_1=6\left[\frac{g_a}{h}\right]^2,$$
$$\alpha_2=\frac{\varepsilon_0 b l_1^4}{2EIg_a^3},\alpha_3=\frac{6}{\Lambda}\left[\frac{g_a}{h}\right]^2,\Omega=\widetilde{\Omega}\tau,\Delta m=\frac{m_p}{\rho A l_1}$$

The Heaviside function and boundary conditions are

$$H_1(x)=\left|H\left(x-\frac{l_1-l_3}{2l_1}\right)-H\left(x-\frac{l_1+l_3}{2l_1}\right)\right| \tag{7}$$

$$\begin{cases}w_1(0,t)=w_1(1,t)=\dfrac{\partial w_1}{\partial x}(0,t)=\dfrac{\partial w_1}{\partial x}(1,t)\\ w_2\left(\dfrac{1-\Lambda}{2},t\right)=w_2\left(\dfrac{1+\Lambda}{2},t\right)=\dfrac{\partial w_2}{\partial x}\left(\dfrac{1-\Lambda}{2},t\right)=\dfrac{\partial w_2}{\partial x}\left(\dfrac{1+\Lambda}{2},t\right)\end{cases} \tag{8}$$

2.2. Static analysis

The deflection of the two microbeams consists of a static component caused by a DC voltage, represented by $w_{s1}(x)$, $w_{s2}(x)$, and a small dynamic component caused by an AC voltage, expressed as $u_1(x, t)$, $u_2(x, t)$.

$$\begin{cases}w_1(x,t)=w_{s1}(x)+u_1(x,t)\\ w_2(x,t)=w_{s2}(x)+u_2(x,t)\end{cases} \tag{9}$$

Substituting Eq. (9) into Eq. (6) and then setting the AC forcing term and the time derivatives equal to zero, we can obtain

$$\begin{cases}\dfrac{\partial^4 w_{s1}}{\partial x^4}=\left[N_1+\alpha_1\displaystyle\int_0^1\left(\dfrac{\partial w_{s1}}{\partial x}\right)^2dx\right]\dfrac{\partial^2 w_{s1}}{\partial x^2}\\ \qquad-\alpha_2 V_c^2 H_1(x)\left(\dfrac{1}{R^2}-\dfrac{2}{R^3}\left(w_{s1}-w_{s2}\right)\right)\\ \dfrac{\partial^4 w_{s2}}{\partial x^4}=\left[N_2+\alpha_3\displaystyle\int_{\frac{1-\Lambda}{2}}^{\frac{1+\Lambda}{2}}\left(\dfrac{\partial w_{s2}}{\partial x}\right)^2dx\right]\dfrac{\partial^2 w_{s2}}{\partial x^2}\\ \qquad-\alpha_2 V_{dc}^2\left(1-2w_{s2}+3w_{s2}^2-4w_{s2}^3\right)\\ \qquad+\alpha_2 V_c^2 H_1(x)\left(\dfrac{1}{R^2}-\dfrac{2}{R^3}\left(w_{s1}-w_{s2}\right)\right)\end{cases} \tag{10}$$

The boundary conditions are

$$\begin{cases}w_{s1}(0)=w_{s1}(1)=\dfrac{\partial w_{s1}}{\partial x}(0)=\dfrac{\partial w_{s1}}{\partial x}(1)=0\\ w_{s2}\left(\dfrac{1-\Lambda}{2}\right)=w_{s2}\left(\dfrac{1+\Lambda}{2}\right)=\dfrac{\partial w_{s2}}{\partial x}\left(\dfrac{1-\Lambda}{2}\right)=\dfrac{\partial w_{s2}}{\partial x}\left(\dfrac{1+\Lambda}{2}\right)=0\end{cases} \tag{11}$$

when the coupling voltage V_c is fixed, the static deflection at the center of the microbeam increases with the applied voltage V_{dc}.

There are many ways to solve the static problems like Differential-Quadrature Method [33] and shooting method [31]. Moreover, another common and powerful method called asymptotic numerical method is adopted here.

$$\begin{cases}w_{s1}(x)=\displaystyle\sum_{i=1}^{N}q_{s1,i}\phi_{1,i}\\ w_{s2}(x)=\displaystyle\sum_{i=1}^{N}q_{s2,i}\phi_{2,i}\end{cases} \tag{12}$$

where $q_{s1,i}$, $q_{s2,i}$ are the i_{th} static generalized coordinate, and $\phi_{1,i}(x)$, $\phi_{2,i}(x)$ are the i_{th} linear undamped mode shape of the straight microbeam 1 and microbeam 2, respectively.

By substituting Eq. (12) into (10), multiplying the mode shapes of $\phi_{1,i}(x)$ and $\phi_{2,i}(x)$, and integrating the two equations from 0 to 1 and

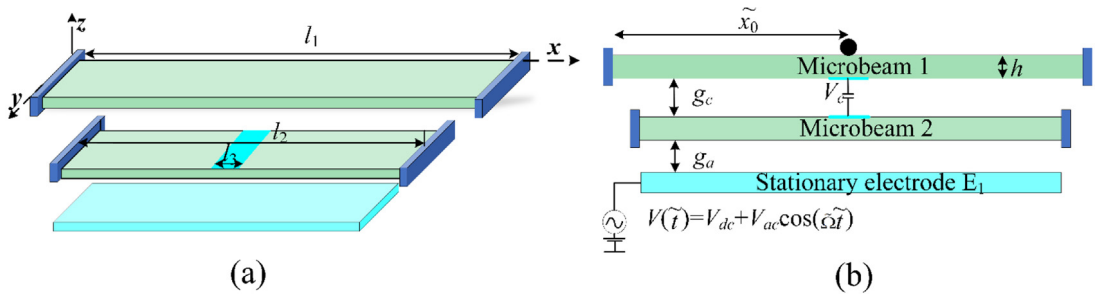

Fig. 1. A scheme of proposed mass sensor. (a) the device; (b) model of two coupled microbeams with added point mass and electrostatic actuation.

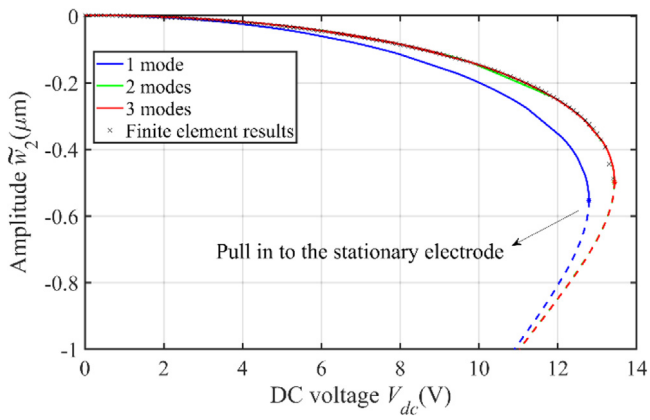

Fig. 2. Variation of the maximum static deflection of the microbeam 2 with respect to the voltage V_{dc} for the coupling voltage $V_c = 5$ V.

from $(1-\Lambda)/2$ to $(1+\Lambda)/2$ respectively, the continuous system can be discretized, while assuming that no axial loads are applied to the microbeam. Since we are interested in the pull-in voltage under static displacement, the number of modes is continuously increased, as shown in Fig. 2 and only the symmetric modes were considered. It can be seen that the solution keeps almost constant when the number of modes reaches two. Though introducing multiple modes can improve precision, it can also complicate the calculation process. Fig. 2 shows that the accuracy is sufficient when the two first symmetric modes are used to predict the pull-in voltage and microbeam deflection, and the result is in good agreement with the finite element. Here, the finite element results are obtained by the software COMSOL Multiphysics [34]. When the coupling voltage of the two microbeams is $V_c = 5$ V, the pull-in voltage is equal to 13.75 V.

2.3. Mode veering analysis

Neglecting the damping and nonlinear terms, the method of modal decomposition is employed to investigate the mode veering point between the Eigen-modes of the presented structure. By substituting Eq. (9) into Eq. (6), the mode veering phenomenon between the curves of the natural frequencies with the change of DC voltage is obtained, as shown in Fig. 3. Here, the coupling voltage $V_c = 5$ V and other structural parameters are listed in Table 1.

During the simulation, we found that the length ratio λ and actuation gap g_a have a significant influence on the mode veering voltage. As shown in Fig. 3(a), reducing the length ratio λ or increasing the actuation gap g_a lead to an increase in the veering voltage.

Fig. 3(b)–(e) show the variation of the frequencies of each mode ($\omega_{1,1}$ and $\omega_{2,1}$) as a function of the DC voltage for different length ratios when the actuation gap $g_a = 1$ μm. When the length of the two microbeams are equal, the natural frequencies are very close and then move away as the DC voltage increases. When the length ratio is less than 0.94, the mode veering point approaches to the pull-in voltage. Here, we choose the length ratio of 0.96 in the next simulation section. With the selected structural parameters, when the value of V_{dc} reaches 8.6 V, the system can reach a balanced state.

2.4. HBM+ANM for periodic solutions

To eliminate the spatial dependence, the Galerkin expansion is used to discretize the nonlinear equations. And the mode shapes of the straight microbeams are used as base functions in the Galerkin procedure [31]. The deflection of each clamped microbeam is approximated by

$$\begin{cases} w_1(x,t) = w_{s1}(x) + \sum_{i=1}^{N_m} q_{1,i}(t)\,\phi_{1,i}(x) \\ w_2(x,t) = w_{s2}(x) + \sum_{i=1}^{N_m} q_{2,i}(t)\,\phi_{2,i}(x) \end{cases} \tag{13}$$

where $q_{1,i}(t)$, $q_{2,i}(t)$ are the i_{th} dynamic generalized coordinate.

By substituting Eq. (13) into Eq. (6), multiplying the mode functions with $\varphi_{1,i}(x)$, $\varphi_{2,i}(x)$, integrating the results from 0 to 1 and from δ_1 to δ_2, respectively, and then subtract the static part, the reduced-order model can be obtained, as deduced in Appendix A.1. For further simplification, a matrix–vector form is introduced [9].

$$\begin{cases} \left[\mathbf{M1_0}+\boldsymbol{\eta}\right]\ddot{\mathbf{q}}_1 + \mathbf{C1_0}\dot{\mathbf{q}}_1 + \mathbf{K1_0}\mathbf{q}_1 - \alpha_1\left[\mathbf{K1_{T1}}+\mathbf{K1_{T0}}\right]\left(T1_1(\mathbf{q}_1)\right. \\ \quad \left. + T1_2(\mathbf{q}_1)\right) - \left[N_1+\alpha_1 T1_0\right]\mathbf{K1_{T1}} = \mathbf{F1}\mathbf{q}_1 - \mathbf{F2}\mathbf{q}_2 \\ \mathbf{M2_0}\ddot{\mathbf{q}}_2 + \mathbf{C2_0}\dot{\mathbf{q}}_2 + \mathbf{K2_0}\mathbf{q}_2 - \alpha_3\left[\mathbf{K2_{T1}}+\mathbf{K2_{T0}}\right]\left(T2_1(\mathbf{q}_2)+T2_2(\mathbf{q}_2)\right) \\ \quad - \left[N_2+\alpha_3 T2_0\right]\mathbf{K2_{T1}} = \mathbf{F2}\mathbf{q}_2 - \mathbf{F1}\mathbf{q}_1 \\ \quad + \alpha_2 V_a^2\left[\mathbf{D_1}-\mathbf{D_0}+\mathbf{S_1}-12\mathbf{S_2}+32\mathbf{S_3}\right] + V_{dc}^2\alpha_2\left[\mathbf{D_0}-2\mathbf{S_1}+3\mathbf{S_2}-4\mathbf{S_3}\right] \end{cases} \tag{14}$$

where $q_1(t) = [q_{1,1}(t), q_{1,2}(t), \ldots, q_{1,Nm}(t)]^T$, $q_2(t)=[q_{2,1}(t), q_{2,2}(t), \ldots, q_{2,Nm}(t)]^T$. The items of matrices $\mathbf{M1}_0$, η, $\mathbf{C1}_0$, $\mathbf{K1}_0$, $\mathbf{K1}_{T0}$, $\mathbf{K1}_{T1}$, $\mathbf{M2}_0$, $\mathbf{C2}_0$, $\mathbf{K2}_0$, $\mathbf{K2}_{T0}$, $\mathbf{K2}_{T1}$, $\mathbf{D}_0$, $\mathbf{D}_1$, $\mathbf{S}_1$, $\mathbf{S}_2$, $\mathbf{S}_3$, $\mathbf{F1}$, $\mathbf{F2}$ are respectively $M1_{0ij}$, η_{ij}, $C1_{0ij}$, $K1_{0ij}$, $K1_{T0ij}$, $K1_{T1ij}$, $M2_{0ij}$, $C2_{0ij}$, $K2_{0ij}$, $K2_{T0ij}$, $K2_{T1ij}$, D_{0ij}, D_{1ij}, S_{1ij}, S_{2ij}, S_{3ij}, and these scalars $T1_1(q_1)$, $T1_2(q_1)$, $T2_1(q_2)$ and $T2_2(q_2)$, all of them are written in Appendix A.2.

The dynamics of the coupled microbeams with quadratic and cubic nonlinearities are obtained by using the method ANM combined with HBM thanks to MANLAB, which is a graphical interactive software that runs in Matlab [35,36] and used for the continuation of solution branches of nonlinear systems. The following three steps are required: the first step and the most important step are to transform the system equations into quadratic terms and then decompose the equation formed in the previous step into the Fourier series by HBM. The last step is to explore the ANM on the resulting system. Subsequently, a detailed description of the first step of the quadratic recast has been

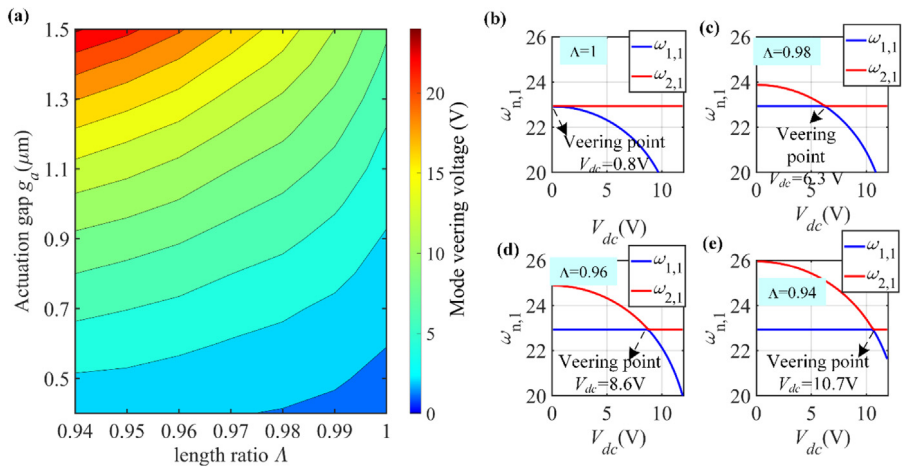

Fig. 3. (a) The influences of length ratio λ and actuation gap g_a on the mode veering voltage; (b), (c), (d), (e) Variation of the frequencies of each mode for the proposed device with respect to the DC voltage for different length ratio λ ($\Lambda = l_2/l_1$, l_1 remains constant).

shown in Eq. (15) and the relevant details of the other two steps have been introduced in [9] and will not be described here.

$$\begin{aligned}
\mathbf{y_1} &= \dot{\mathbf{q}}_1 && (size\ N_m)\\
\mathbf{y_2} &= \dot{\mathbf{q}}_2 && (size\ N_m)\\
\mathbf{z_1} &= \dot{\mathbf{y}}_1 && (size\ N_m)\\
\mathbf{z_2} &= \dot{\mathbf{y}}_2 && (size\ N_m)\\
\mathbf{K1_{Ttot}} &= \mathbf{K1_{T1}} + \mathbf{K1_{T0}} && (size\ N_m^2)\\
\mathbf{K2_{Ttot}} &= \mathbf{K2_{T1}} + \mathbf{K2_{T0}} && (size\ N_m^2)\\
T1 &= T1_1(q_1) + T1_2(q_1) && (size\ 1)\\
T2 &= T2_1(q_2) + T2_2(q_2) && (size\ 1)
\end{aligned} \tag{15}$$

and Eq. (14) can be rewritten as in Box I, where $\mathbf{X}=(\mathbf{q_1}, \mathbf{q_2}, \mathbf{y_1}, \mathbf{y_2}, \mathbf{z_1}, \mathbf{z_2}, \mathbf{K1_{Ttot}}$, is the unknown vector of size $N_{eq} = 6N_m + 2N_m^2 + 2$, the constant vector is c, $l(.)$ and $m(.)$ are linear vector-valued operators with respect to $\mathbf{X}$, and $q(.,.)$ is a quadratic vector-valued operator with respect to $\mathbf{X}$. Here, the Galerkin discretization term $N_m = 2$ uses two modes to simplify calculation without loss of computational accuracy [37].

3. Numerical results

The traditional mass sensitivity is mainly dependent on the ratio of the resonance frequency shift to the corresponding added mass. Here, the ratio of the amplitude shift can be utilized as an output metric. The two sensitivities can be expressed as

$$S_{\omega_i} = \left|\frac{\omega_i - \omega_i^0}{\omega_i^0}\right| \Big/ \Delta m \tag{17}$$

$$S_a = \left|\left(\frac{w_2}{w_1} - \frac{w_2^0}{w_1^0}\right) \Big/ \frac{w_2^0}{w_1^0}\right| \Big/ \Delta m \tag{18}$$

where $S_{\omega i}$ and S_a represents the sensitivity based on the shift of the resonant frequency and amplitude ratio, respectively, ω_i^0 is the frequency of balance state, ω_i is the frequency after the mass added, w_1, w_2 is the amplitude after the mass added of resonator 1 and resonator 2, respectively, w_1^0, w_2^0 is the amplitude of balance state of resonator 1 and resonator 2, respectively.

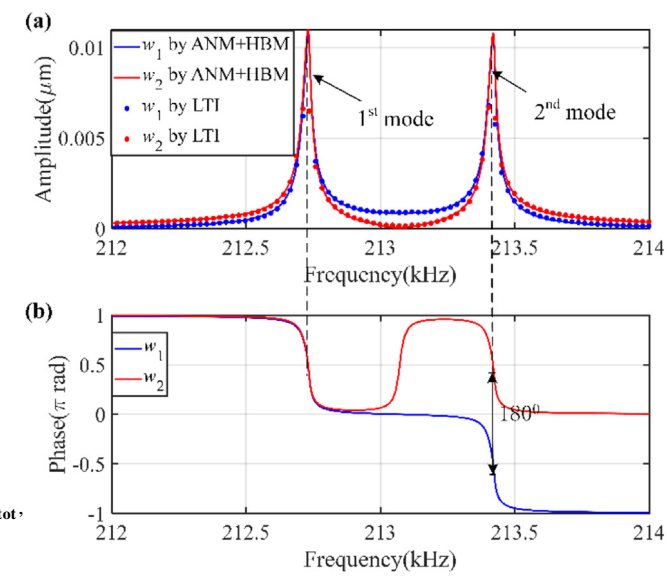

Fig. 4. Amplitude (a) and phase–frequency (b) responses of the two resonators in a balanced state with $V_c = 5$ V, $V_{dc} = 8.56$, $V_{ac} = 0.0001$ V.

3.1. Linear behaviors

Assuming that the two clamped microbeams have the same quality factor (Q = 8000) and the coupling voltage V_c is fixed at 5.0 V, the AC voltage is fixed at V_{ac} = 0.0001 V, the system becomes balanced when V_{dc} is equal to 8.56 V. Thereafter, the peaks of the two modes are equal regardless of unequal lengths of resonator 1 and resonator 2 at the veering point, as shown in Fig. 4(a). The two resonators undergo linear vibrations. The response of the 1st mode is in-phase and that of the 2nd mode is out-of-phase in Fig. 4(b).

According to previous reports [32], the two resonators can vibrate in linear behavior when the applied voltage V_{ac} is less than 0.18 mV. To investigate the effect of the voltage V_{ac} on sensitivity in the linear behavior range, the different voltage of V_{ac} is applied from 0.05 mV to 0.18 mV. The added mass at the midpoint of resonator 1 is increasing from 0 pg to 3 pg.

With the increase of the V_{ac}, the relative shift of amplitude ratio is slightly improved. It can be noted in Fig. 5(a), (b) that the relative shift of amplitude ratio as the output metric is more sensitive for the 2nd mode, the sensitivity of the linear region is approximately

$$
\begin{array}{lcllll}
\dot{\mathbf{q}}_{\mathbf{1}} & = & & \mathbf{y}_{\mathbf{1}} & & \\
\dot{\mathbf{q}}_{\mathbf{2}} & = & & \mathbf{y}_{2} & & \\
\dot{\mathbf{y}}_{\mathbf{1}} & = & & \mathbf{z}_{\mathbf{1}} & & \\
\dot{\mathbf{y}}_{2} & = & & \mathbf{z}_{2} & & \\
0 & = & -\mathbf{K1}_{\mathbf{T0}} & \mathbf{K1}_{\mathbf{Ttot}} - \mathbf{K1}_{\mathbf{T1}} & & \\
0 & = & -\mathbf{K2}_{\mathbf{T0}} & \mathbf{K2}_{\mathbf{Ttot}} - \mathbf{K2}_{\mathbf{T2}} & & \\
0 & = & & T1 - T1_1\left(q_1\right) & -T1_2\left(q_1\right) & \\
0 & = & & T2 - T2_1\left(q_2\right) & -T2_2\left(q_2\right) & \\
0 & = & & \left[\mathbf{M1_0} + \boldsymbol{\eta}\right]\mathbf{z_1} + \mathbf{C1_0}\mathbf{y_1} + \mathbf{K1_0}\mathbf{q_1} - \left[N_1 + \alpha_1 T1_0\right]\mathbf{K1_{T1}} - F1q_1 + F2q_2 & -\alpha_1\mathbf{K1}_{\mathbf{Ttot}}T1 & \\
0 & = & -\alpha_2 V_a^2\left[\mathbf{S_1} - 12\mathbf{S_2} + 32\mathbf{S_3} - \mathbf{D_0}\right] - V_{dc}^2\alpha_2\left[\mathbf{D_0} - 2\mathbf{S_1} + 3\mathbf{S_2} - 4\mathbf{S_3}\right] & \mathbf{M2_0}\mathbf{z}_2 + \mathbf{C1_0}\mathbf{y}_2 + \mathbf{K2_0}\mathbf{q_2} - \left[N_2 + \alpha_3 T2_0\right]\mathbf{K2_{T1}} - F2\mathbf{q_2} + F1\mathbf{q_1} - \alpha_2 V_a^2\mathbf{D_1} & -\alpha_3\mathbf{K2}_{\mathbf{Ttot}}T2 & \\
\underbrace{\phantom{m\left(\dot{\mathbf{X}}\right)}}_{} & = & \underbrace{\phantom{c\left(\boldsymbol{\Omega}\right)}}_{} & \underbrace{\phantom{l\left(\mathbf{X}\right)}}_{} & \underbrace{\phantom{\mathrm{q}\left(\mathbf{X},\mathbf{X}\right)}}_{} & \\
m\left(\dot{\mathbf{X}}\right) & = & c\left(\boldsymbol{\Omega}\right) & + \quad l\left(\mathbf{X}\right) & + \quad \mathrm{q}\left(\mathbf{X},\mathbf{X}\right) &
\end{array}
\tag{16}
$$

Box I.

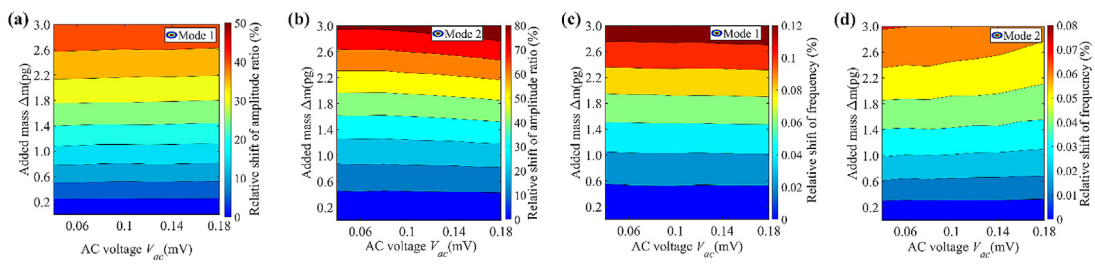

Fig. 5. Variation of the relative shift of the resonance frequency and amplitude ratio with respect to Δm and V_{ac}. (a), (c) Sensitivity for linear behavior at the 1st mode in terms of amplitude ratio and frequency shift; (b), (d) Sensitivity for linear behavior at the 2nd mode in terms of amplitude ratio and frequency shift.

19.45%/pg. In contrast, the relative frequency shift as the output metric is more sensitive for the 1st mode, and the sensitivity is approximately 0.031%/pg as shown in Fig. 5(c), (d). The relative change of the amplitude ratio is more than 627 times higher than the relative shift in its resonance frequency.

3.2. Nonlinear behavior

The two resonators can vibrate in linear behavior when a low AC voltage is applied. Actually, an AC voltage of more than 0.18 mV enables the device to reach the critical amplitude, which it is the transition amplitude from the linear to the nonlinear behavior [38–40]. For example, when the voltage of V_{ac} is set to be 0.4 mV, the influence of nonlinear behaviors on the sensitivity is analyzed with a fixed quality factor and an unchanged coupling voltage V_c. Here, the DC voltage V_{dc} = 8.583 V is re-adjusted to ensure that the system is operating in a balanced state. The frequency response curves of the two modes are shown in Fig. 6. From Fig. 6(b), it can be seen that the two microbeams are oscillating at symmetric and the anti-symmetric modes. From Fig. 6(a), it is worth noting that solid line curves obtained by ANM+HBM are in good agreement with the points simulated by the LTI, thus validating the solving methods. For mass sensing, the changing ratio of the highest amplitude is selected as an output metric in sensitivity calculation.

Fig. 7 shows the sensitivities when the device is operating in the nonlinear behavior, for the two different modes respectively. Further observations for the simulation results can be divided into two aspects: (i) the sensitivity outputs of resonators are substantially depicted by the frequency shift, and the relative change of the resonance frequency of the 1st mode is much larger than that of the 2nd mode; (ii) contrary to the aforementioned results, the relative shift of amplitude ratio of the

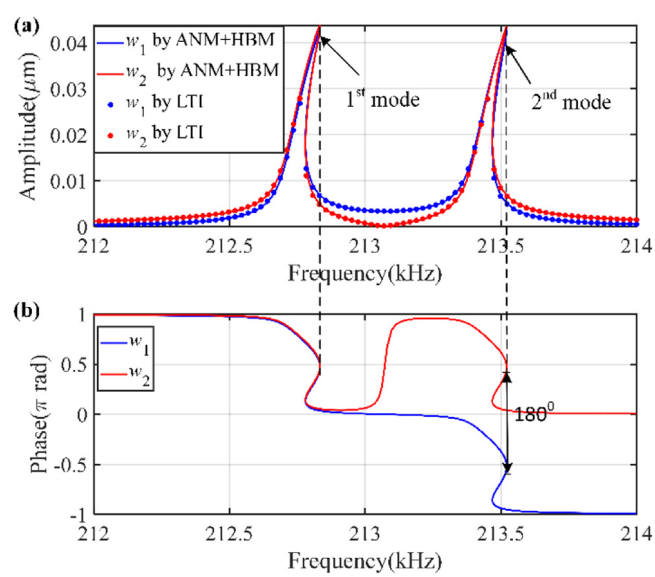

Fig. 6. Amplitude (a) and phase (b) responses of two microbeams resonating in a balanced state with V_c = 5 V, V_{dc} = 8.583, V_{ac} = 0.0004 V.

1st mode is smaller compared to the 2nd mode. As reported in [41], the 2nd mode is localized in the stiffer resonator.

The relative shift of amplitude ratio as the output metric is more sensitive for the 2nd mode, the sensitivity of the linear region is approximately 47.23%/pg in Fig. 7(b). For the relative frequency shift, the sensitivity is approximately 0.035%/pg in Fig. 7(c). As predicted,

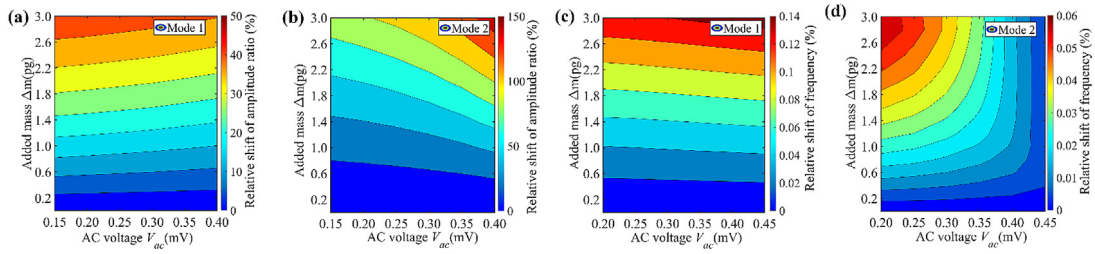

Fig. 7. Variation of th relative shift of the resonance frequency and amplitude ratio with respect to Δm and V_{ac}. (a), (c) Sensitivity for nonlinear behavior at the 1st mode in terms of amplitude ratio and frequency shift; (b), (d) Sensitivity for nonlinear behavior at the 2nd mode in terms of amplitude ratio and frequency shift.

the relative change of the amplitude ratio is more than three orders of magnitude higher than the relative shift in its resonance frequency.

Figs. 6(b) and 7(b) show that compared with the device operating in a linear behavior, the sensitivity is improved 242.83% when operating in the nonlinear state in the 2nd mode. Furthermore, as the voltage V_{ac} increases, the amplitude ratio as the output metric has a larger detection range than the frequency shift output in the 2nd mode.

In summary, utilizing the amplitude ratio of the 2nd mode as the output metric permits the achievement of higher sensitivity compared to the 1st mode, and the sensitivity can be further improved when the device is operating in the nonlinear state.

3.3. Adjustability of the sensitivity by electrostatic coupling stiffness

Actually, the sensitivity is significantly affected by the electrostatic coupling stiffness, which is controlled by the voltage. The two clamped–clamped microbeams are electrostatically coupled, and the variable stiffness can be easily regulated. This coupling method can overcome the defects of traditional mechanical coupling to obtain low coupling stiffness. When the AC voltage is fixed at V_{ac} = 0.0004 V, the effects of the value of coupling strength V_c on the amplitude ratio are shown in Fig. 8. The sensitivity can be significantly improved by reducing the coupling strength. Precisely, it is increased by 15.79 times when the coupling voltage V_c is decreased from 10.0 V to 4.0 V in Fig. 8(a). Thus, the sensitivity enhancement can be tuned by adjusting the coupling strength V_c.

The first two natural frequencies variations with respect the coupling strength are shown in Fig. 8(b). Although decreasing the coupling strength V_c can increase sensitivity, the first natural frequency is gradually increased close to the second eigenfrequency by reducing the coupling strength. When the coupling voltage is less than 4 V, the device will generate mode aliasing, which limits the proposed sensing technique, based on the eigenstate variation.

4. Influences of the geometric parameters

The effect of different geometric parameters on sensitivity is investigated, such as position of added mass x_0, length ratio λ ($\lambda = l_2/l_1$), gap ratio (R), Numerical analysis has been conducted for using the amplitude ratio of the 2nd mode as the output metric, which is much higher than that of the 1st mode. Also, the sensitivity can be further improved when the device is operating in a nonlinear state.

4.1. Effects of the position of added mass on sensitivity

The effect of the dimensionless position of added mass x_0 on sensitivity is investigated. Fig. 9(a) shows the variation of the sensitivity with respect to the dimensionless position x_0. It can be noticed that there is a large effect of the dimensionless position x_0 on the sensitivity. With the dimensionless position x_0 of the added mass vary from 0.1 to 0.5, the sensitivity can be increased by 89.24 times. Since the vibration mode is symmetrical, the sensitivity is optimal when the dimensionless position $x_0 = 0.5$. From the frequency response curve of the resonators shown in Fig. 9(b)–(c), it can be seen that under the same driving force and mass disturbance, the amplitude gradually increases. For many mass sensors, to accurately measure the target analyte, a thin film with a surface adsorption function is attached to the beam. Thus, in order to obtain high sensitivity, the surface adsorption film should be stuck in the middle of the microbeam 1.

4.2. Effects of the length ratio on sensitivity

The system is balanced by adjusting V_{dc} at a constant AC voltage (V_{ac} = 0.4 mV) for different length ratios. The effects of length ratio on the sensitivity are shown in Fig. 10(a). By setting the length of resonator 1 (l_1 = 200 μm) to be constant, the length ratio can be changed by varying the length of resonator 2.

It can be seen that the sensitivity of 2nd mode changes inversely with the length ratio. And the sensitivity will be lowest when the two lengths are equals. Hence, the unequal length sensor is more sensitive than a sensor based on periodic structures. Although the reduction in length ratio can increase the sensitivity, it cannot be infinitely small, and as the length ratio decreases, the voltage V_{dc} of the balanced state is gradually close to pull-in voltage in Fig. 3. The smallest length ratio here is 0.94. Fig. 10(b)–(c) are the frequency responses of the resonators, it was found that under the same mass disturbance, when the length ratio is 0.94, the amplitude is larger and the pull-in phenomenon is more likely to occur.

4.3. Effects of the gap ratio on sensitivity

We consider investigating the effect of the actuation gap g_a and the coupling gap g_c between the two microbeams on the sensitivity. Fig. 11(a) shows the variation of the sensitivity with the gap g_c increases and g_a is constant 1 μm. It can be noted that there is a huge effect of the gap g_c on the sensitivity. When the gap between the two microbeams g_c is increased from 2 μm up to 2.5 μm, the resulted sensitivity can be increased by 4.39 times, which is reasonable since increasing the gap ratio will decrease the coupling strength. However, when the gap g_c exceeds 2.5 μm, mode aliasing occurs, which can be considered as the upper bound limit for sensitivity improvement for the considered design parameters.

In contrast, when the gap g_c between the two microbeams is set constant at 2 μm, the variation of the actuation gap g_a between 0.6 μm and 1.5 μm has little effects on the sensitivity as shown in Fig. 11(b). Through the above analysis, the sensitivity is mainly affected by the coupling gap g_c between the two microbeams.

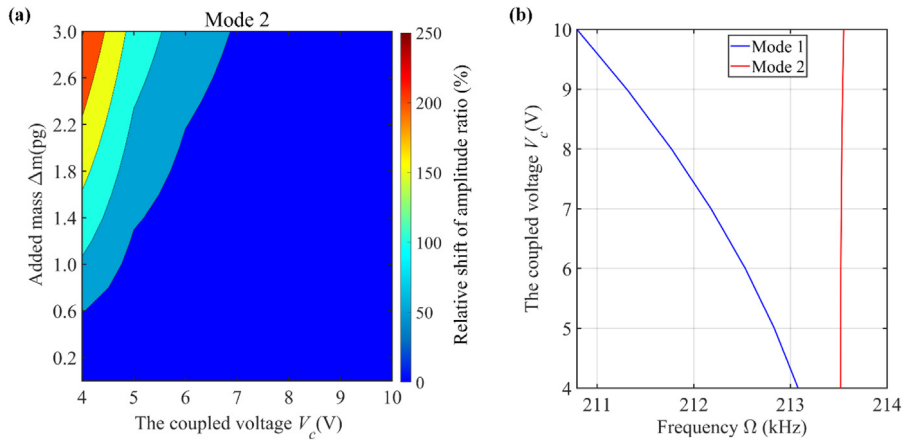

Fig. 8. (a) Variation of the sensitivity with respect to the coupling voltage (V_c); (b) Variation of the natural frequencies with respect to the coupling voltage (V_c).

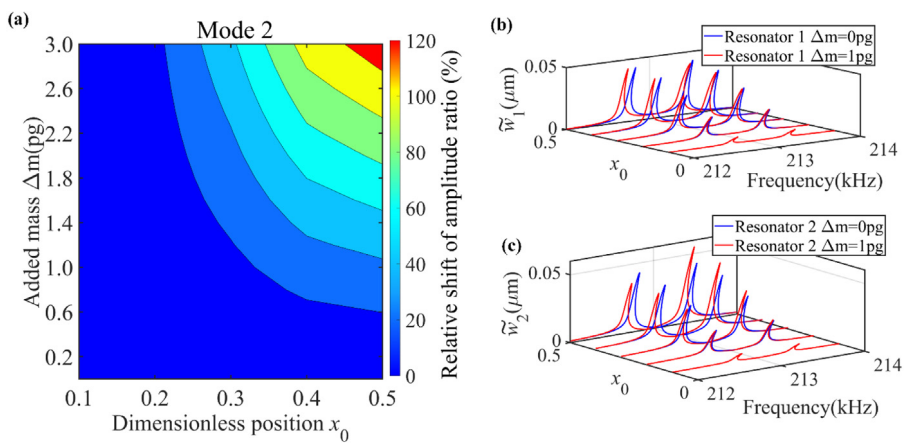

Fig. 9. (a) Variation of the sensitivity with respect to the dimensionless position x_0 of added mass; (b), (c) Frequency responses of the resonators 1 and 2 for different dimensionless positions x_0 and an added mass of 1pg.

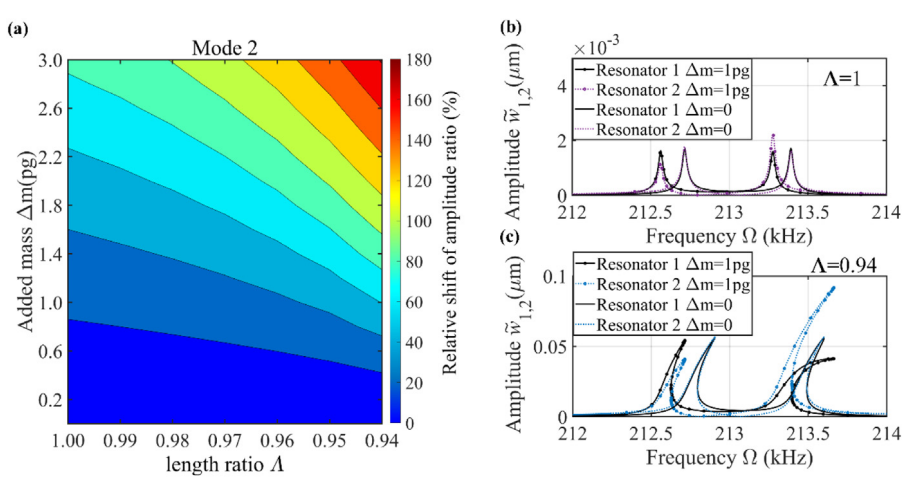

Fig. 10. (a) Variation of the sensitivity with respect to the length of resonator 2; (b), (c) Frequency responses of the resonators 1 and 2 in nonlinear behavior for an added mass of 1pg.

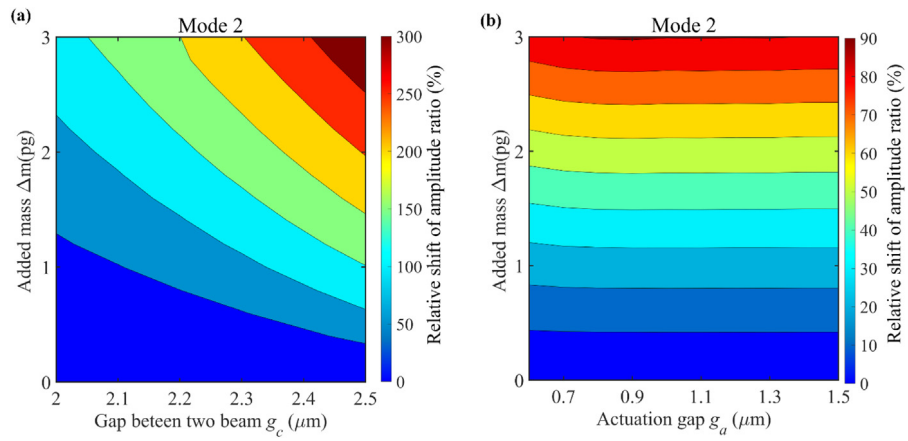

Fig. 11. Variation of the second mode sensitivity with the gap ratio. (a) the value g_a is set constant at 1 μm and the coupling gap between the two microbeams g_c is changed; (b) the value g_c is set constant at 2 μm and the actuation gap g_a is changed.

5. Conclusion

In this paper, we have demonstrated the design of mass sensor by introducing the mode localization of two electrostatically coupled clamped–clamped microbeams of different lengths. Only the shorter microbeam is actuated by a combined AC–DC voltage, which can be adjusted to overcome the mechanical defects of asymmetry while driving the device beyond its critical Duffing amplitude.

Firstly, the equation of motion of the system considering the quadratic and cubic nonlinearities was established and solved by the method of ANM and HBM, and the long-term integration method is applied to validate the effectiveness of the solving procedure. Secondly, the sensor operating in linear and nonlinear regimes can be controlled by the AC voltage applied to the shorter microbeam. More importantly, the sensitivity can be further improved by nonlinear behavior. Thirdly, utilizing the amplitude ratio of the 2nd mode as the output metric enables the device to reach higher sensitivity compared to the 1st mode, and the sensitivity can be improved up to three orders of magnitude compared to the common frequency shift as an output metric. Finally, the effects of several design parameters on sensitivity have been revealed. The sensitivity can be modulated by adjusting the length ratio, coupling voltage and gap ratio, e.g., reducing the length ratio or weakening the coupling strength can improve the sensitivity, and among them, reducing the coupling strength has the greatest effect on sensitivity improvement below the onset of mode aliasing phenomenon.

Declaration of competing interest

The authors declare that they have no known competing financial interests or personal relationships that could have appeared to influence the work reported in this paper.

CRediT authorship contribution statement

Ming Lyu: Methodology, Conceptualization, Software, Writing - original draft. **Jian Zhao:** Conceptualization, Methodology, Writing - review & editing, Supervision. **Najib Kacem:** Conceptualization, Writing - review & editing. **Pengbo Liu:** Validation. **Bin Tang:** Software. **Zhuang Xiong:** Validation. **Hongxi Wang:** Investigation. **Yu Huang:** Investigation, Writing - review & editing.

Acknowledgments

This work was supported in part by the National Natural Science Foundation of China (Grant No. 51575088, 61874019, U1930206), and project of State Key Laboratory of Structural Analysis for Industrial Equipment, China (Grant No. GZ19202). This work was also performed in cooperation with EUR EIPHI program, Europe (Contract No. ANR 17-EURE-0002).

Appendix

A.1. Reduced order model

$$
\begin{aligned}
&\left(1+\Delta m\phi_{1,\mathrm{i}}\left(x_0\right)\phi_{1,\mathrm{j}}\left(x_0\right)\right)\ddot{q}_{1,i}+c\dot{q}_{1,i}+\omega_{non1,i}^2 q_{1,i}\\
&-\alpha_1\sum_{j=1}^{N_m} q_{s1,j}\int_0^1 \phi_{1,i}\phi''_{1,j}dx\times\left\{\sum_{m=1}^{N_m}\sum_{n=1}^{N_m} q_{1,m}q_{1,n}\int_0^1 \phi''_{1,m}\phi'_{1,n}dx\right.\\
&\left.+2\sum_{m=1}^{N_m}\sum_{n=1}^{N_m} q_{1,m}q_{s1,n}\int_0^1 \phi'_{1,m}\phi'_{1,n}dx\right\}\\
&-\alpha_1\sum_{j=1}^{N_m} q_{1,j}\int_0^1 \phi_{1,i}\phi''_{1,j}dx\times\left\{\sum_{m=1}^{N_m}\sum_{n=1}^{N_m} q_{1,m}q_{1,n}\int_0^1 \phi'_{1,m}\phi'_{1,n}dx\right.\\
&\left.+2\sum_{m=1}^{N_m}\sum_{n=1}^{N_m} q_{1,m}q_{s1,n}\int_0^1 \phi'_{1,m}\phi'_{1,n}dx+\sum_{m=1}^{N_m}\sum_{n=1}^{N_m} q_{s1,m}q_{s1,n}\int_0^1 \phi'_{1,m}\phi'_{1,n}dx\right\}\\
&=\frac{2\alpha_2 V_c^2\sum_{j=1}^{N_m}\int_0^1 H_1(x)\phi_{1,i}\phi_{1,j}dx}{R^3}q_{1,j}\\
&-\frac{2\alpha_2 V_c^2\sum_{j=1}^{N_m}\int_0^1 H_1(x)\phi_{1,i}\phi_{2,j}dx}{R^3}q_{2,j}+N_1\sum_{j=1}^{N_m} q_{1,j}\int_0^1 \phi_{1,i}\phi''_{1,j}dx
\end{aligned}
\tag{19}
$$

$$
\begin{aligned}
&\ddot{q}_{2,i}+c\dot{q}_{2,i}+\omega_{non2,\mathrm{i}}^2 q_{2,i}-\alpha_3\sum_{j=1}^{N_m} q_{s2,j}\int_{\delta_1}^{\delta_2}\phi_{2,i}\phi''_{2,j}dx\\
&\times\left(\sum_{m=1}^{N_m}\sum_{n=1}^{N_m} q_{2,m}q_{2,n}\int_{\delta_1}^{\delta_2}\phi'_{2,m}\phi'_{2,n}dx+2\sum_{m=1}^{N_m}\sum_{n=1}^{N_m} q_{2,m}q_{s2,n}\int_{\delta_1}^{\delta_2}\phi'_{2,m}\phi'_{2,n}dx\right)\\
&-\alpha_3\sum_{j=1}^{N_m} q_{2,j}\int_{\delta_1}^{\delta_2}\phi_{2,i}\phi''_{2,j}dx\times\left(\sum_{m=1}^{N_m}\sum_{n=1}^{N_m} q_{2,m}q_{2,n}\int_{\delta_1}^{\delta_2}\phi'_{2,m}\phi'_{2,n}dx\right.\\
&\left.+2\sum_{m=1}^{N_m}\sum_{n=1}^{N_m} q_{2,m}q_{s2,n}\int_{\delta_1}^{\delta_2}\phi'_{2,m}\phi'_{2,n}dx+\sum_{m=1}^{N_m}\sum_{n=1}^{N_m} q_{s2,m}q_{s2,n}\int_{\delta_1}^{\delta_2}\phi'_{2,m}\phi'_{2,n}dx\right)
\end{aligned}
$$

$$
\begin{aligned}
&= \frac{2V_c^2\alpha_2 \sum_{j=1}^{N_m}\left(\int_{\delta_1}^{\delta_2} H_1(x)\,\phi_{2,i}\phi_{2,j}\,dx\right)}{R^3} q_{2,j} \\
&- \frac{2V_c^2\alpha_2 \sum_{j=1}^{N_m}\left(\int_{\delta_1}^{\delta_2} H_1(x)\,\phi_{1,j}\phi_{2,i}\mathrm{d}x\right)}{R^3} q_{1,j} \\
&+ N_2 \sum_{j=1}^{N_m} q_{2,j}\int_{\delta_1}^{\delta_2}\phi_{2,i}\phi''_{2,j}\mathrm{d}x - \alpha_2 V_a^2\int_{\delta_1}^{\delta_2}\phi_{2,i}\mathrm{d}x \\
&+ 2\alpha_2 V_a^2\left[\sum_{j=1}^{N_m} q_{2,j}\int_{\delta_1}^{\delta_2}\phi_{2,j}\phi_{2,i}\mathrm{d}x + \sum_{j=1}^{N_m} q_{s2,j}\int_{\delta_1}^{\delta_2}\phi_{2,i}\phi_{2,j}\mathrm{d}x\right. \\
&- 6\sum_{j=1}^{N_m}\sum_{k=1}^{N_m} q_{s2,j}q_{s2,k}\int_{\delta_1}^{\delta_2}\phi_{2,i}\phi_{2,j}\phi_{2,k}\mathrm{d}x \\
&\left.+ 16\sum_{j=1}^{N_m}\sum_{k=1}^{N_m}\sum_{l=1}^{N_m} q_{s2,j}q_{s2,k}q_{s2,l}\int_{\delta_1}^{\delta_2}\phi_{2,i}\phi_{2,j}\phi_{2,k}\phi_{2,l}\mathrm{d}x\right] \\
&+ V_{dc}^2\alpha_2\left[\int_{\delta_1}^{\delta_2}\phi_{2,i}\mathrm{d}x - 2\sum_{j=1}^{N_m} q_{s2,j}\int_{\delta_1}^{\delta_2}\phi_{2,i}\phi_{2,j}\mathrm{d}x\right. \\
&+ 3\sum_{j=1}^{N_m}\sum_{k=1}^{N_m} q_{s2,j}q_{s2,k}\int_{\delta_1}^{\delta_2}\phi_{2,i}\phi_{2,j}\phi_{2,k}\mathrm{d}x \\
&\left.- 4\sum_{j=1}^{N_m}\sum_{k=1}^{N_m}\sum_{l=1}^{N_m} q_{s2,j}q_{s2,k}q_{s2,l}\int_{\delta_1}^{\delta_2}\phi_{2,i}\phi_{2,j}\phi_{2,k}\phi_{2,l}\mathrm{d}x\right]
\end{aligned}
\tag{20}
$$

where $V_a^2 = \left(V_{dc} + V_{ac}\cos(\Omega t)\right)^2$. Since the DC voltage is generally much higher than the AC voltage, the squared term of AC voltage is neglected and hence $V_a^2 = \left(V_{dc} + V_{ac}\cos(\Omega t)\right)^2 \approx V_{dc}^2 + 2V_{dc}V_{ac}\cos(\Omega t)$, $\delta_1 = (1-\Lambda)/2$, $\delta_2 = (1+\Lambda)/2$, $q_{1,i}$, $q_{2,i}$ are unknown functions related to time.

A.2. The integration parameters of Eq. (14)

$$
\begin{aligned}
&\mathrm{M1}_{0ij} = \delta 1_{ij} \\
&\mathrm{M2}_{0ij} = \delta 2_{ij} \\
&C1_{0ij} = c_j \mathrm{M1}_{0ij} \\
&C2_{0ij} = c_j \mathrm{M2}_{0ij} \\
&K1_{0ij} = \omega_{non1,\mathrm{j}}^2 \\
&K2_{0ij} = \omega_{non2,\mathrm{j}}^2 \\
&K1_{T0ij} = \sum_{j=1}^{N_m}\left(\int_0^1 \phi_{1,i}\phi''_{1,j}\mathrm{d}x\right) q_{s1,j} \\
&K1_{T1ij} = \sum_{j=1}^{N_m}\left(\int_0^1 \phi_{1,i}\phi''_{1,j}\mathrm{d}x\right) q_{1,j} \\
&T1_0 = \sum_{m=1}^{N_m}\sum_{n=1}^{N_m}\left(\int_0^1 \phi'_{1,m}\phi'_{1,n}dx\right) q_{s1,m}q_{s1,n} \\
&T1_1(q_1) = 2\sum_{m=1}^{N_m}\sum_{n=1}^{N_m}\left(\int_0^1 \phi'_{1,m}\phi'_{1,n}dx\right) q_{1,m}q_{s1,n} \\
&T1_2(q_1) = \sum_{m=1}^{N_m}\sum_{n=1}^{N_m}\left(\int_0^1 \phi'_{1,m}\phi'_{1,n}dx\right) q_{1,m}q_{1,n} \\
&D_{0ij} = \int_{\delta_1}^{\delta_2}\phi_{2,i}\mathrm{d}x \\
&D_{1ij} = 2\left(\int_{\delta_1}^{\delta_2}\sum_{j=1}^{N_m}\phi_{2,j}\phi_{2,i}\mathrm{d}x\right) q_{2,j} \\
&S_{1ij} = 2\sum_{j=1}^{N_m}\left(\int_{\delta_1}^{\delta_2}\phi_{2,i}\phi_{2,j}\mathrm{d}x\right) q_{s2,j} \\
&S_{2ij} = \sum_{j=1}^{N_m}\sum_{k=1}^{N_m}\left(\int_{\delta_1}^{\delta_2}\phi_{2,i}\phi_{2,j}\phi_{2,k}\mathrm{d}x\right) q_{s2,j}q_{s2,k} \\
&S_{3ij} = \sum_{j=1}^{N_m}\sum_{k=1}^{N_m}\sum_{l=1}^{N_m}\left(\int_{\delta_1}^{\delta_2}\phi_{2,i}\phi_{2,j}\phi_{2,k}\phi_{2,l}\mathrm{d}x\right) q_{s2,j}q_{s2,k}q \\
&K2_{T0ij} = \sum_{j=1}^{N_m}\left(\int_{\delta_1}^{\delta_2}\phi_{2,i}\phi''_{2,j}\mathrm{d}x\right) q_{s2,j}, \\
&K2_{T1ij} = \sum_{j=1}^{N_m}\left(\int_{\delta_1}^{\delta_2}\phi_{2,i}\phi''_{2,j}\mathrm{d}x\right) q_{2,j} \\
&T2_0 = \sum_{m=1}^{N_m}\sum_{n=1}^{N_m}\left(\int_{\delta_1}^{\delta_2}\phi'_{2,\mathrm{m}}\phi'_{2,\mathrm{n}}\mathrm{d}x\right) q_{s2,\mathrm{m}}q_{s2,\mathrm{n}} \\
&\eta_{ij} = \Delta m\phi_{1,i}(x_0)\,\phi_{1,j}(x_0) \\
&T2_1(\mathrm{q}_2) = 2\sum_{m=1}^{N_m}\sum_{n=1}^{N_m}\left(\int_{\delta_1}^{\delta_2}\phi'_{2,\mathrm{m}}\phi'_{2,\mathrm{n}}\mathrm{d}x\right) q_{2,\mathrm{m}}q_{s2,\mathrm{n}} \\
&T2_2(\mathrm{q}_2) = \sum_{m=1}^{N_m}\sum_{n=1}^{N_m}\left(\int_{\delta_1}^{\delta_2}\phi'_{2,\mathrm{m}}\phi'_{2,\mathrm{n}}\mathrm{d}x\right) q_{2,\mathrm{m}}q_{2,\mathrm{n}} \\
&F1_i = \frac{2\alpha_2 V_c^2 \sum_{j=1}^{N_m}\left(\int_0^1 H_1(x)\,\phi_{1,i}\phi_{1,j}\,dx\right)}{R^3} \\
&F2_i = \frac{2V_c^2\alpha_2 \sum_{j=1}^{N_m}\left(\int_{\delta_1}^{\delta_2} H_1(x)\,\phi_{1,j}\phi_{2,i}\mathrm{d}x\right)}{R^3}
\end{aligned}
\tag{21}
$$

References

[1] J. Fritz, M.K. Baller, H.P. Lang, H. Rothuizen, P. Vettiger, E. Meyer, H.J. Guntherodt, C. Gerber, J.K. Gimzewski, Translating biomolecular recognition into nanomechanics, Science 288 (2000) 316–318, http://dx.doi.org/10.1126/science.288.5464.316.

[2] Y. Arntz, J.D. Seelig, H.P. Lang, J. Zhang, P. Hunziker, J.P. Ramseyer, E. Meyer, M. Hegner, C. Gerber, Label-free protein assay based on a nanomechanical cantilever array, Nanotechnology 14 (2003) 86–90, http://dx.doi.org/10.1088/0957-4484/14/1/319.

[3] H. Zhang, M.S. Marma, S.K. Bahl, E.S. Kim, C.E. McKenna, Sequence specific label-free DNA sensing using film-bulk-acoustic-resonators, IEEE Sens. J. 7 (2007) 1587–1588, http://dx.doi.org/10.1109/jsen.2007.905035.

[4] K.M. Hansen, H.F. Ji, G.H. Wu, R. Datar, R. Cote, A. Majumdar, T. Thundat, Cantilever-based optical deflection assay for discrimination of DNA single-nucleotide mismatches, Anal. Chem. 73 (2001) 1567–1571, http://dx.doi.org/10.1021/ac0012748.

[5] H.T. Yu, P.C. Xu, X.Y. Xia, D.W. Lee, X.X. Li, Micro-/nanocombined gas sensors with functionalized mesoporous thin film self-assembled in batches onto resonant cantilevers, IEEE Trans. Ind. Electron. 59 (2012) 4881–4887, http://dx.doi.org/10.1109/Tie.2011.2173094.

[6] G.H. Wu, R.H. Datar, K.M. Hansen, T. Thundat, R.J. Cote, A. Majumdar, Bioassay of prostate-specific antigen (PSA) using microcantilevers, Nat. Biotechnol. 19 (2001) 856–860, http://dx.doi.org/10.1038/nbt0901-856.

[7] T.P. Burg, S.R. Manalis, Suspended microchannel resonators for biomolecular detection, Appl. Phys. Lett. 83 (2003) 2698–2700, http://dx.doi.org/10.1063/1.1611625.

[8] J. Zhao, Y. Zhang, R. Gao, S. Liu, A new sensitivity improving approach for mass sensors through integrated optimization of both cantilever surface profile and cross-section, Sensors Actuators B 206 (2015) 343–350, http://dx.doi.org/10.1016/j.snb.2014.09.033.

[9] S. Souayeh, N. Kacem, Computational models for large amplitude nonlinear vibrations of electrostatically actuated carbon nanotube-based mass sensors, Sensors Actuators A 208 (2014) 10–20, http://dx.doi.org/10.1016/j.sna.2013.12.015.

[10] W.H. Zhang, K.L. Turner, Application of parametric resonance amplification in a single-crystal silicon micro-oscillator based mass sensor, Sensors Actuators A 122 (2005) 23–30, http://dx.doi.org/10.1016/j.sna.2004.12.033.

[11] T.J. Anderson, A.H. Nayfeh, B. Balachandran, Experimental verification of the importance of the nonlinear curvature in the response of a cantilever beam, J. Vib. Acoust. 118 (1996) 21–27, http://dx.doi.org/10.1115/1.2889630.

[12] T.J. Anderson, A.H. Nayfeh, B. Balachandran, Coupling between high-frequency modes and a low-frequency mode: Theory and experiment, Nonlinear Dynam. 11 (1996) 17–36, http://dx.doi.org/10.1007/BF00045049.

[13] H.M. Zhang, J.M. Zhong, W.Z. Yuan, J. Yang, H.L. Chang, Ambient pressure drift rejection of mode-localized resonant sensors, in: Proc IEEE Micr Elect, 2017, pp. 1095–1098, http://dx.doi.org/10.1109/MEMSYS.2017.7863604.

[14] M. Spletzer, A. Raman, A.Q. Wu, X. Xu, R. Reifenberger, Ultrasensitive mass sensing using mode localization in coupled microcantilevers, Appl. Phys. Lett. 88 (2006) 254102, http://dx.doi.org/10.1063/1.2216889.

[15] V. Walter, G. Bourbon, P. Le Moal, N. Kacem, J. Lardiès, Electrostatic actuation to counterbalance the manufacturing defects in a MEMS mass detection sensor using mode localization, Proc. Eng. 168 (2016) 1488–1491, http://dx.doi.org/10.1016/j.proeng.2016.11.431.

[16] N. Kacem, V. Walter, G. Bourbon, P. Le Moal, J. Lardiès, Mode veering and internal resonance in mechanically coupled nanocantilevers under electrostatic actuation, Proc. Eng. 168 (2016) 924–928, http://dx.doi.org/10.1016/j.proeng.2016.11.307.

[17] T. Rabenimanana, V. Walter, N. Kacem, P. Le Moal, G. Bourbon, J. Lardiès, Mass sensor using mode localization in two weakly coupled MEMS cantilevers with different lengths: Design and experimental model validation, Sensors Actuators A 295 (2019) 643–652, http://dx.doi.org/10.1016/j.sna.2019.06.004.

[18] M. Pandit, C. Zhao, G. Sobreviela, A. Mustafazade, A.A. Seshia, Coupled nonlinear MEMS resonators for sensing, in: P IEEE Int Freq Cont, 2018, pp. 203–206, https://doi.org/10.1109/FCS.2018.8597571.

[19] J.Y.P. Thiruvenkatanathan, J.E.-Y. Lee, A.A. Seshia, Enhancing parametric sensitivity using mode localization in electrically coupled MEMS resonator, in: 15th International Conference on Solid-State Sensors, Actuators and Microsystems. Transducers, 2009, pp. 2350–2353, https://doi.org/10.1109/SENSOR.2009.5285444.

[20] Y. Wang, C. Zhao, C. Wang, D. Cerica, M. Baijot, Q. Xiao, S. Stoukatch, M. Kraft, A mass sensor based on 3-DOF mode localized coupled resonator under atmospheric pressure, Sensors Actuators A 279 (2018) 254–262, http://dx.doi.org/10.1016/j.sna.2018.06.028.

[21] H. Zhang, B. Li, W. Yuan, M. Kraft, H. Chang, An acceleration sensing method based on the mode localization of weakly coupled resonators, J. Microelectromech. Syst. 25 (2016) 286–296, http://dx.doi.org/10.1109/jmems.2015.2514092.

[22] C. Zhao, G.S. Wood, J. Xie, H. Chang, S.H. Pu, M. Kraft, A force sensor based on three weakly coupled resonators with ultrahigh sensitivity, Sensors Actuators A 232 (2015) 151–162, http://dx.doi.org/10.1016/j.sna.2015.05.011.

[23] S. Marquez, M. Alvarez, J.A. Plaza, L.G. Villanueva, C. Dominguez, L.M. Lechuga, Asymmetrically coupled resonators for mass sensing, Appl. Phys. Lett. 111 (2017) http://dx.doi.org/10.1063/1.5003023.

[24] S. Ramakrishnan, B. Balachandran, Energy localization and white noise-induced enhancement of response in a micro-scale oscillator array, Nonlinear Dynam. 62 (2010) 1–16, http://dx.doi.org/10.1007/s11071-010-9694-6.

[25] A.J. Dick, B. Balachandran, C.D. Mote Jr., Localization in microresonator arrays: Influence of natural frequency tuning, J. Comput. Nonlinear Dyn. 5 (2009) 11, http://dx.doi.org/10.1115/1.4000314.

[26] B. Balachandran, E. Perkins, T. Fitzgerald, Response localization in micro-scale oscillator arrays: influence of cubic coupling nonlinearities, Int. J. Dyn. Control 3 (2014) 183–188, http://dx.doi.org/10.1007/s40435-014-0139-9.

[27] D.F. Wang, K. Chatani, T. Ikehara, R. Maeda, Mode localization analysis and characterization in a 5-beam array of coupled nearly identical micromechanical resonators for ultra-sensitive mass detection and analyte identification, Microsyst. Technol. 18 (2012) 1923–1929, http://dx.doi.org/10.1007/s00542-012-1520-2.

[28] C. Zhao, G.S. Wood, S.H. Pu, M. Kraft, A mode-localized MEMS electrical potential sensor based on three electrically coupled resonators, J. Sens. Sens. Syst. 6 (2017) 1–8, http://dx.doi.org/10.5194/jsss-6-1-2017.

[29] M. Pandit, C. Zhao, G. Sobreviela, S. Du, X. Zou, A. Seshia, Utilizing energy localization in weakly coupled nonlinear resonators for sensing applications, J. Microelectromech. Syst. 28 (2019) 182–188, http://dx.doi.org/10.1109/jmems.2019.2894953.

[30] P. Thiruvenkatanathan, J. Yan, A.A. Seshia, Common mode rejection in electrically coupled MEMS resonators utilizing mode localization for sensor applications, in: 2009 Joint Conference of the 22nd European Frequency and Time Forum and the IEEE International Frequency Control Symposium, IEEE, 2009, pp. 358–363, http://dx.doi.org/10.1109/Freq.2009.5168201.

[31] M.I. Younis, E.M. Abdel-Rahman, A. Nayfeh, A reduced-order model for electrically actuated microbeam-based MEMS, J. Microelectromech. Syst. 12 (2003) 672–680, http://dx.doi.org/10.1109/jmems.2003.818069.

[32] L. Li, J. Han, Q. Zhang, C. Liu, Z. Guo, Nonlinear dynamics and parameter identification of electrostatically coupled resonators, Int. J. Non Linear Mech. 110 (2019) 104–114, http://dx.doi.org/10.1016/j.ijnonlinmec.2018.12.008.

[33] F. Najar, S. Choura, E.M. Abdel-Rahman, S. El-Borgi, A.H. Nayfeh, Dynamics of variable-geometry electrostatic microactuators, J. Micromech. Microeng. (2006) 2449–2457, http://dx.doi.org/10.1088/0960-1317/16/11/028.

[34] COMSOL, http://www.comsol.com/.

[35] S. Karkar, B. Cochelin, C. Vergez, A high-order, purely frequency based harmonic balance formulation for continuation of periodic solutions: The case of non-polynomial nonlinearities, J. Sound Vib. 332 (2013) 968–977, http://dx.doi.org/10.1016/j.jsv.2012.09.033.

[36] B. Cochelin, C. Vergez, A high order purely frequency-based harmonic balance formulation for continuation of periodic solutions, J. Sound Vib. 324 (2009) 243–262, http://dx.doi.org/10.1016/j.jsv.2009.01.054.

[37] S. Baguet, V.N. Nguyen, C. Grenat, C.H. Lamarque, R. Dufour, Nonlinear dynamics of micromechanical resonator arrays for mass sensing, Nonlinear Dynam. 95 (2018) 1203–1220, http://dx.doi.org/10.1007/s11071-018-4624-0.

[38] N. Kacem, S. Hentz, D. Pinto, B. Reig, V. Nguyen, Nonlinear dynamics of nanomechanical beam resonators: improving the performance of NEMS-based sensors, Nanotechnology 20 (2009) 275501, http://dx.doi.org/10.1088/0957-4484/20/27/275501.

[39] N. Kacem, J. Arcamone, F. Perez-Murano, S. Hentz, Dynamic range enhancement of nonlinear nanomechanical resonant cantilevers for highly sensitive NEMS gas/mass sensor applications, J. Micromech. Microeng. 20 (2010) 045023, http://dx.doi.org/10.1088/0960-1317/20/4/045023.

[40] N. Kacem, S. Hentz, S. Baguet, R. Dufour, Forced large amplitude periodic vibrations of non-linear mathieu resonators for microgyroscope applications, Int. J. Non-Linear Mech. 46 (2010) 1347–1355, http://dx.doi.org/10.1016/j.ijnonlinmec.2011.07.008.

[41] B.K. Hammad, E.M. Abdel-Rahman, A.H. Nayfeh, Modeling and analysis of electrostatic MEMS filters, Nonlinear Dynam. 60 (2009) 385–401, http://dx.doi.org/10.1007/s11071-009-9603-z.